

ARTICLE

Open Access

Direct extraction of respiratory information from pulse waves using a finger-inspired flexible pressure sensor system

Xikuan Zhang¹, Jin Chai², Lingxiao Xu³, Shixuan Mei⁴, Xin Wang^{5,6}, Yunlong Zhao^{5,6}, Chenyang Xue⁷, Yongjun Wang⁸, Danfeng Cui^{1✉}, Zengxing Zhang^{5,6}, Haiyan Zhang^{8✉} and Libo Gao^{5,6✉}

Abstract

The long-term monitoring of respiratory status is crucial for the prevention and diagnosis of respiratory diseases. However, existing continuous respiratory monitoring devices are typically bulky and require either chest strapping or proximity to the nasal area, which compromises user comfort and may disrupt the monitoring process. To overcome these challenges, we have developed a flexible, attachable, lightweight, and miniaturized system designed for extended wear on the wrist. This system incorporates signal acquisition circuitry, a mobile client, and a deep neural network, facilitating long-term respiratory monitoring. Specifically, we fabricated a highly sensitive ($11,847.24 \text{ kPa}^{-1}$) flexible pressure sensor using a screen printing process, which is capable of functioning beyond 70,000 cycles. Additionally, we engineered a bidirectional long short-term memory (BiLSTM) neural network, enhanced with a residual module, to classify various respiratory states including slow, normal, fast, and simulated breathing. The system achieved a dataset classification accuracy exceeding 99.5%. We have successfully demonstrated a stable, cost-effective, and durable respiratory sensor system that can quantitatively collect and store respiratory data for individuals and groups. This system holds potential for everyday monitoring of physiological signals and healthcare applications.

Introduction

Breathing constitutes a fundamental physiological process, essential for sustaining life¹. Respiratory dysfunction often signals various underlying pathological conditions^{2,3}. As such, continuous monitoring of respiratory status is crucial for the prevention of respiratory diseases and for guiding clinical care. Respiratory monitoring techniques are broadly categorized into two main groups: direct monitoring and indirect inference methods^{4,5}. Direct monitoring captures respiratory signals by tracking thoracic and abdominal movements as well as airflow changes^{6–9}. Although this approach can provide a precise reflection of

respiratory status, its usage is often hampered by discomfort and impracticality for prolonged periods.

Conversely, indirect inference methods, which have gained considerable attention recently, predominantly estimate respiratory status by analyzing physiological signals such as heart rate variability and pulse waveform to determine respiratory frequency^{10–12}. Motin M. A introduced a novel approach for monitoring respiratory function using principal component analysis combined with the ensemble empirical mode decomposition (EEMD-PCA) algorithm, applied to photoplethysmography (PPG) signals from public databases, aimed at estimating respiratory frequency¹¹. Despite their non-invasive nature and suitability for long-term monitoring, indirect methods may lack the precision of direct methods in estimating respiratory rates. Thus, refining the accuracy of these indirect techniques remains a significant challenge.

The human pulse wave provides critical insights into both physiological and pathological processes^{13,14}. Research has demonstrated a significant correlation

Correspondence: Danfeng Cui (cuidanfeng@nuc.edu.cn) or Haiyan Zhang (zhy_zhanghaiyan@163.com) or Libo Gao (lbgao@xmu.edu.cn)

¹Key Laboratory of Instrumentation Science and Dynamic Measurement Ministry of Education, North University of China, Taiyuan 030051, China
²College of Chemistry and Chemical Engineering, Xiamen University, Xiamen 361105, China

Full list of author information is available at the end of the article
These authors contributed equally: Xikuan Zhang, Jin Chai

© The Author(s) 2025



Open Access This article is licensed under a Creative Commons Attribution-NonCommercial-NoDerivatives 4.0 International License, which permits any non-commercial use, sharing, distribution and reproduction in any medium or format, as long as you give appropriate credit to the original author(s) and the source, provide a link to the Creative Commons licence, and indicate if you modified the licensed material. You do not have permission under this licence to share adapted material derived from this article or parts of it. The images or other third party material in this article are included in the article's Creative Commons licence, unless indicated otherwise in a credit line to the material. If material is not included in the article's Creative Commons licence and your intended use is not permitted by statutory regulation or exceeds the permitted use, you will need to obtain permission directly from the copyright holder. To view a copy of this licence, visit <http://creativecommons.org/licenses/by-nc-nd/4.0/>.

between characteristics of the pulse wave and respiratory activity^{15–17}. Changes in the amplitude, baseline, and frequency of the pulse wave have been associated with variations in respiratory activity¹⁸. Respiratory sinus arrhythmia (RSA) exemplifies this relationship, highlighting the influence of respiration on heart rate regulation¹⁹. Previous research has utilized signal quality indices to improve the accuracy of respiratory frequency estimation directly from pulse characteristics^{20–24}. However, this method lacks stability during long-term monitoring. Traditional methods for classifying respiratory states often rely on simple threshold techniques, which, while straightforward, are limited in their ability to accurately determine respiratory states²⁵. The application of advanced computational methods such as machine learning and deep learning has shown promise in enhancing classification accuracy. Techniques including support vector machines²⁶, random forests²⁷, and one-dimensional convolutional neural networks (1D-CNNs)^{28,29} have been used for data classification, although they struggle with modeling temporally variable data. Recurrent neural networks (RNNs)³⁰ excel in capturing temporal dynamics but face challenges related to gradient training. In contrast, bidirectional long short-term memory networks (BiLSTM)³¹ have demonstrated improved sequence representation capabilities. Additionally, integrating BiLSTM with ResNet³² is anticipated to overcome gradient issues and enhance feature extraction in complex respiratory data analysis.

In this study, we developed a wearable wristband device designed for precise, continuous monitoring of respiration. The core element of this system is a highly sensitive flexible pressure sensor, characterized by a sensitivity of $11,847.24 \text{ kPa}^{-1}$, a detection range from 1 to 50 kPa, a rapid response time of only 37 ms, and a durability exceeding 70,000 cycles. This device proficiently monitors the radial artery pulse during respiration and preprocesses the pulse signal, enabling differentiation among slow, normal, and fast breathing rhythms, as well as simulated respiratory states. Additionally, we evaluated the performance of BiLSTM and ResNet-BiLSTM neural networks; our findings indicated that the ResNet-BiLSTM provided superior training stability and achieved a classification accuracy of 99.5%. Furthermore, the integrated sensing platform, comprising sensors, flexible printed circuit boards, and mobile applications, supports long-term respiratory monitoring. This integration facilitates personalized health management and aids in the treatment of respiratory diseases.

Results and discussion

System design and integration

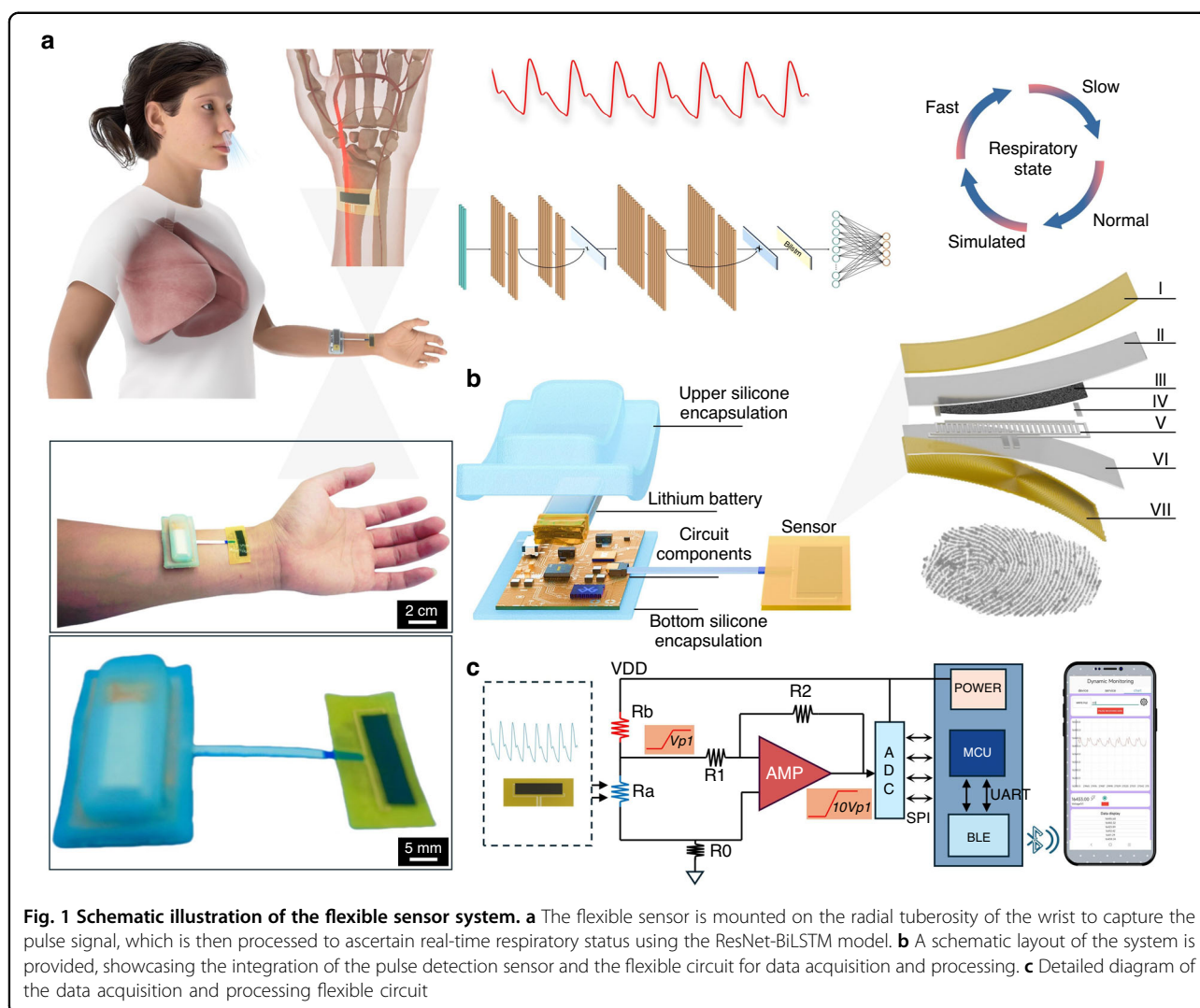
Figure 1a, b depicts the configuration of the respiratory monitoring system, which includes two primary components:

a flexible sensor for pulse detection and a flexible circuit with encapsulation for data acquisition and processing. The system's integrated flexible design not only enhances wearability—thereby improving pulse data monitoring—but also ensures user comfort. The pulse sensor's thickness is merely 300 μm , which simplifies its attachment. The fabrication process of the pulse sensor, as shown in Fig. 1b, begins with the sequential printing of an electrode layer composed of interdigital silver electrodes (Fig. 1b-V) and a spacer layer made from thermoplastic polyurethane (TPU) ink (Fig. 1b-IV) on a TPU substrate (Fig. 1b-VI). This assembly is then aligned with another TPU substrate (Fig. 1b-II), which has been previously printed with a sensitive layer composed of CNT-based material (Fig. 1b-III). The device is ultimately fully encapsulated using a PDMS film (Fig. 1b-I, VII), which not only enhances comfort against the skin but also extends the device's operational lifespan. Laser etching technology is used to create fingerprint-like, ring-shaped structures on the back layer of the PDMS film (Fig. 1b-VII), improving the sensor's surface texture and mechanical adhesion³³. Figure 1b further illustrates the encapsulation process of the flexible circuit board (FPCB). The FPCB and sensor are connected via a flexible cable, powered by a rechargeable lithium-ion battery, and encapsulated with silicone, resulting in a microsystem that is highly flexible and lightweight (9 g), thereby minimizing the physical and psychological burden on the user³⁴.

Figure 1c depicts the schematic diagram of a flexible circuit designed for data acquisition and processing. This circuit, as outlined in Fig. S1, comprises a MCU module, a Bluetooth module, an ADC module, and a power supply module. The pulsation of the radial artery prompts a variation in the sensor signal. This variation is amplified and then processed by a 24-bit high-precision ADC (AD7760). The power module includes a 3.7 V rechargeable lithium-ion battery and a Type-C charging port, incorporating a TP4057 charging chip. The microcontroller unit (ESP32) is responsible for data handling, storage, and communication. It transmits the processed data through a Bluetooth Low Energy (BLE) chip (BG22C224) to an application for display purposes. Additionally, Fig. S2 offers both a three-dimensional view and a detailed schematic of the circuit components.

Operating principle and algorithm design

The radial pulse serves as a direct indicator of myocardial pumping strength³⁵. During systole, when the left ventricle contracts, the pulse of blood is propelled from the aorta to the radial artery, manifesting as a detectable pulse at the wrist (Fig. 1a). A flexible sensor, affixed to the radial tuberosity of the wrist, enables precise pulse measurement in an optimal location without the need for a medical professional. Analysis of the pulse wave allows for the measurement of heart rate changes synchronized with



respiratory phases, termed respiration-induced fluctuation in ventricular filling (RIFV), respiration-induced alterations in cardiac output (RIAV), and respiration-induced variations in pulse baseline (RIIV). Additionally, a bidirectional long and short-term memory network (BiLSTM), in conjunction with multiple residual networks (ResNet), is employed to analyze temporal features and distinguish between four respiratory states: slow, normal, fast, and simulated breathing. The incorporation of ResNet enhances the capture of complex spatial data, thereby improving the understanding and operational training of BiLSTM. This integration also addresses the issue of vanishing gradients, thereby enhancing the efficiency and performance of the network during training sessions. By capturing pulse signals and integrating them with a deep learning network (ResNet-BiLSTM), the system achieves an impressive overall classification accuracy of 99.5% on the dataset. This performance results in stable, long-term monitoring of respiratory status.

Comparative analyses with similar studies underscore that this research introduces an advanced respiratory sensor system that is not only wearable and comfortable but also capable of long-term monitoring without requiring specialized physician assistance for localization. Furthermore, it is characterized by high accuracy, as documented in Table S1^{25–29,36–46}.

Sensor and circuit encapsulation preparation

To ensure stable and continuous monitoring of wrist pulse signals, a flexible piezoresistive sensor was developed. Figure 2a delineates the methodology utilized in the sensor's preparation. The surface of the TPU film is treated with plasma to eliminate contaminants, thereby enhancing the adhesion of the subsequently printed materials. The sensor is fabricated by sequentially depositing a silver electrode layer and a TPU spacer layer onto the TPU film via a screen printing technique, as illustrated in Fig. S3a. Following this, a sensitive material

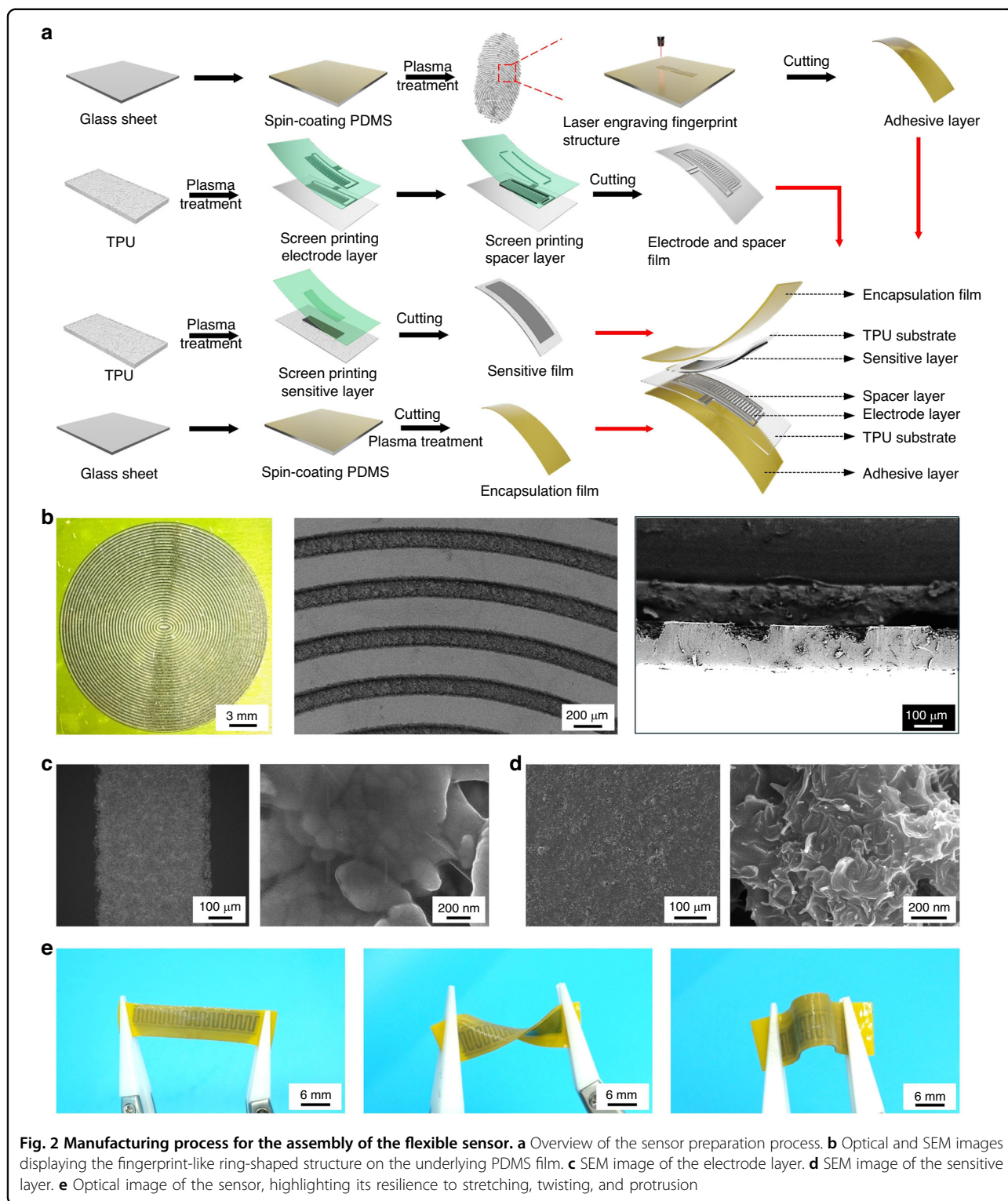


Fig. 2 Manufacturing process for the assembly of the flexible sensor. **a** Overview of the sensor preparation process. **b** Optical and SEM images displaying the fingerprint-like ring-shaped structure on the underlying PDMS film. **c** SEM image of the electrode layer. **d** SEM image of the sensitive layer. **e** Optical image of the sensor, highlighting its resilience to stretching, twisting, and protrusion

—similar to that used in our previous work⁴⁷—is printed onto another plasma-treated TPU film using the same screen printing process (Fig. S3b). The assembly is then fully encapsulated with a plasma-treated PDMS film, topped with a fingerprint-like PDMS layer that has

undergone laser etching and further plasma treatment (Figs. S4 and S5). Figure 2b presents cross-sectional and in-plane microscopic images of the finalized structure. An evaluation of the sensor’s sensitivity and linearity, with variations in ring spacings (Fig. S6) and widths (Fig. S7),

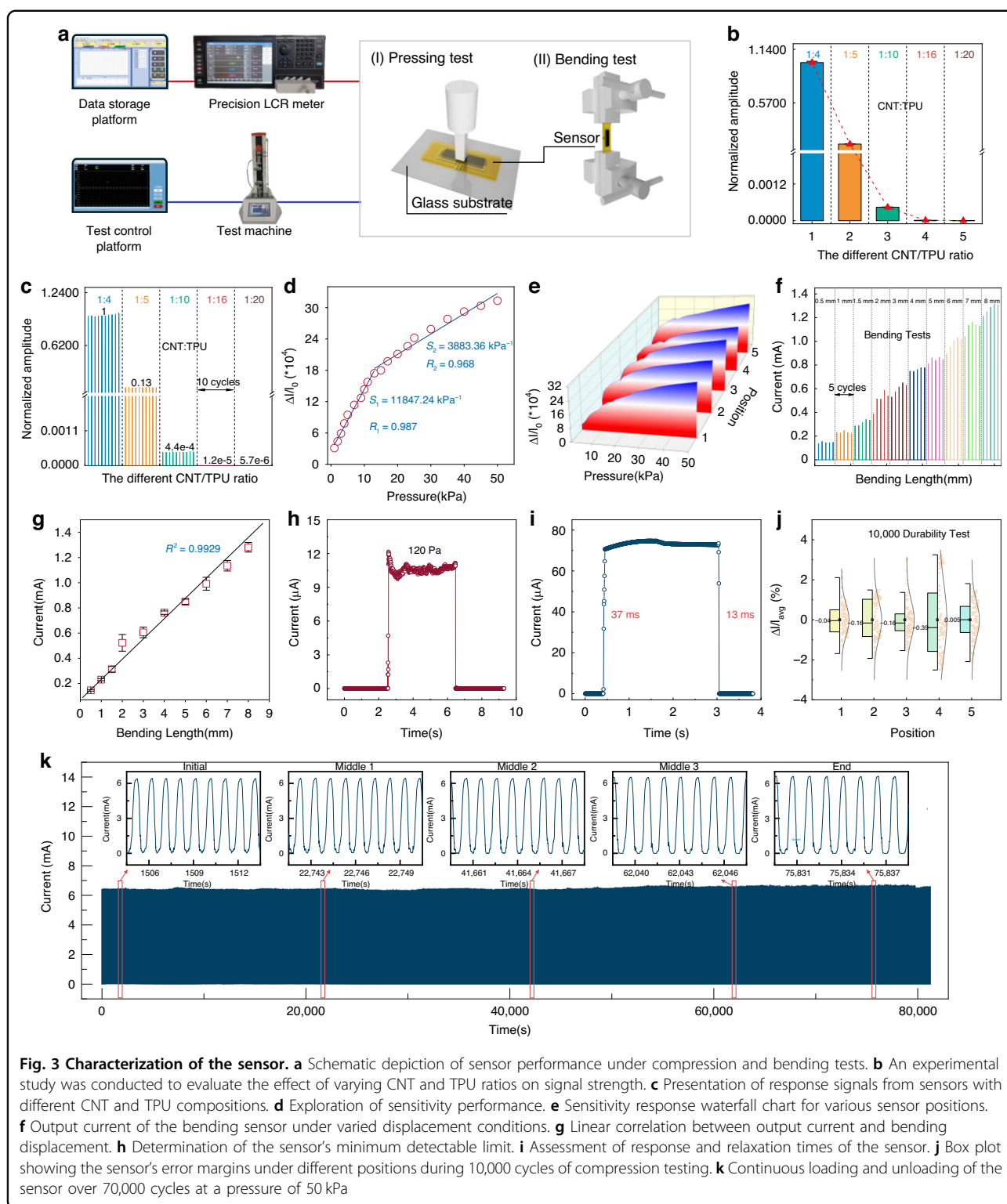
revealed that optimal performance is achieved with a ring width of 200 μm and a spacing of 150 μm . Comparative analyses of the response and relaxation times across different configurations of ring spacings (Fig. S8) and widths (Fig. S9) indicated negligible differences. The sensor demonstrates remarkable flexibility, effectively enduring mechanical stresses such as stretching, bending, twisting, and arching, as evidenced in Figs. 2e and S10. This flexibility ensures a snug fit over the radial tuberosity of the wrist, maintaining direct contact with the skin and thereby enhancing the stability and accuracy of the signal detection. Additionally, the microstructural integrity of the interdigital electrode layer and the sensitive layer was examined (Fig. 2c, d), revealing no significant structural changes compared to those prepared 1 month earlier (Fig. S11). The elemental composition of both the sensitive and interdigital electrode layers (C, N, O, with the addition of Ag in the electrode layer, Figs. S12 and S13) was analyzed using an energy dispersive X-ray spectrometer (EDS). Results confirmed that there were no substantial changes in the composition compared to samples analyzed 1 month prior (Figs. S14 and S15), with the elemental ratios remaining stable (Figs. S16 and S17). We conducted a comparative analysis of the sensitivity, linearity, response time, and relaxation time between a newly prepared sensor and a counterpart fabricated 1 month prior. The analysis revealed that the newly prepared sensor demonstrated enhanced sensitivity and linearity, which can be ascribed to an increased carbon content in its sensitive layer (Figs. 3d and S16, S18). Additionally, we assessed the response and relaxation times of both sensors across ten trials each. The data indicated that the sensor prepared 1 month ago exhibited superior response and relaxation times, likely due to a higher concentration of silver in its electrode layer (Figs. S17 and S19). These observed performance discrepancies are presumably the result of variations in the sensor fabrication processes. The implementation of standardized equipment and more precise manufacturing techniques could potentially reduce these variations. Despite these differences, the overall performance disparity between the two sensors is minimal and does not adversely affect the sensor's typical functionality. Our findings suggest that both the sensitive and interdigital electrode layers maintain robust long-term stability, which is essential for the reliable and continuous monitoring of human physiological signals over prolonged periods.

The circuit packaging was engineered using inverted mold technology and was encapsulated with a mold silicone resin⁴⁸ (Fig. S20). A digital optical image, depicted in Fig. S21, illustrates the circuit package under various mechanical stresses including protrusion, bending, stretching, and twisting. The FPCB demonstrated exceptional bending properties (Fig. S22). Following

encapsulation with silicone, the device not only proved to be stretchable but also comfortable to wear, ensuring strong adhesion to the skin surface of the arm (Fig. S23). This enhanced adhesion was evident in Fig. S24, which highlighted the device's lightweight and flexible nature, enabling a highly comfortable fit and excellent wear resistance, crucial for long-term data monitoring on the forearm.

Device characterization

The performance of the flexible pressure sensor was rigorously evaluated, as depicted in Fig. 3a. The high-precision dynamic electrical testing platform is composed of several critical components: testing control apparatus, data storage units, a precision LCR meter, and a testing machine. The sensors underwent pressure and bending tests facilitated by an electric translation fixture. This testing machine is specifically engineered to apply periodic forces and displacement amplitudes, effectively simulating real-world scenarios. The LCR meter meticulously records the output signals, such as sensor current, thereby providing comprehensive data regarding the sensor's performance across various testing conditions. Through investigating the impact of the CNTs/TPU ratio on the sensor's efficacy, an optimal ratio of 1:4 was established. A statistical histogram of the normalized current output amplitude at a pressure of 50 kPa was constructed (Fig. 3b), revealing that the sensor's signal output peaked under the 1:4 doping ratio condition (Fig. 3c). The sensor demonstrated exceptional sensitivity across a pressure range from 1 to 50 kPa, with a sensitivity of 11,847.24 kPa^{-1} within the 0–13 kPa range and 3883.36 kPa^{-1} throughout the linear operating range of 13–50 kPa (Fig. 3d). Unlike traditional single pulse sensors, which require medical professional intervention to identify the optimal pulse location and thus may limit broader application, our sensor features a straightforward design enabling user-driven tactile interaction with the radial tuberosity of the wrist. To accommodate the pulse regions of different individuals' wrists, the sensor was designed with an effective detection area of 5.5 mm \times 24.8 mm, encompassing five pulse-sensing regions (Fig. S25). Pressure testing across these five sensing zones indicated an effective and consistent response at all locations (Figs. 3e and S26). The bending response of the flexible sensor was also assessed, with bending displacements ranging from 0.5 mm to 8 mm (Fig. 3f); the output current was observed to increase linearly with bending displacement (Fig. 3g). Moreover, the sensor exhibits an exceptionally low detection limit of approximately 120 Pa (Fig. 3h) and is capable of detecting forces significantly below 1 kPa⁴⁹. It also demonstrated a rapid response time of 37 ms and a relaxation time of 13 ms, as illustrated in Fig. 3i. Long-term stability was tested by



subjecting the sensor to a pressure of 50 kPa for 70,000 cycles, with no significant signal degradation observed, thereby demonstrating its excellent cyclic stability (Figs. 3k and S27). Furthermore, after subjecting the

sensor to more than 10,000 cycles at pressures in the five sensing regions, only minimal peak deviation of the current signal was detected (Fig. 3j). These properties affirm that the sensor is well-suited for long-term applications

and meets the criteria for high precision and responsiveness required in pulse monitoring.

Sensor application

Figure 4a illustrates the specific setup utilized for acquiring pulse and respiration data. Before the collection of these signals, volunteers were required to remain stationary for 2 min to stabilize their physiological state, as depicted in Fig. 4a-I and further demonstrated in Supplemental Movie 1. Instructions were given to ensure that participants placed their arms flat on the table, maintained relaxed wrists, and kept their fingers naturally curved, as shown in Fig. 4a-V. Each volunteer was outfitted with a commercial respiratory sensor on the chest and a long-term respiratory monitoring system on the forearm. Additionally, a medical-grade airbag wristband, calibrated to 15 kPa pressure, was positioned on the wrist to exert controlled pressure on the wrist sensor (Fig. 4a-IV). A key component of the setup was a flexible sensor affixed to the radial styloid process of the wrist, secured with medical tape. The system included mobile and computer terminals capable of displaying and storing both pulse (Fig. 4a-III) and respiratory data (Fig. 4a-II) in real time. This functionality allows for the immediate analysis of the collected signals to identify and discard any anomalous data. During respiratory activities, the expansion and contraction of the chest cavity induce alterations in the circulatory system's blood flow. These variations manifest as changes in the amplitude, frequency, and baseline of the pulse waveform, correlating with the RIAV, RIFV, and RIIV features, which are detailed in Fig. 4b.

To analyze the respiratory status of the volunteers, a 32-s sample comprising pulse and respiration data was selected. The baseline drift in the pulse signal was corrected using an envelope recognition algorithm. Subsequently, a sliding window algorithm facilitated the identification of peaks and valleys, and the extraction of RIAV, RIFV, and RIIV features from the pulse signals, as illustrated in Fig. S28. The initial sampling rates for pulse and respiration data were 100 Hz and 50 Hz, respectively. These time series data were then downsampled to a frequency of 5 Hz to compile the final dataset. In this study, 13 volunteers contributed to the data collection, during which their respiratory states were monitored across three distinct levels: slow, normal, and fast breathing. Figure 4d displays the corresponding pulse and respiration data for these states. Additionally, Figs. 4e and S29 depict the interaction between respiration and pulse over a 100-s interval, demonstrating the impact of different respiratory states on this relationship. Analysis of the energy distribution in the time-frequency images across various respiratory states revealed substantial differences, indicating a correlation between respiratory and pulse rates

for each state. Figure 4c shows the respiratory frequency distribution for the different states, which can be summarized as follows: slow breathing at approximately 6 breaths per minute (bpm), normal breathing at approximately 15 bpm, and fast breathing at approximately 30 bpm. However, significant overlap in the respiratory frequencies of these states results in low classification accuracy when employing the threshold method to differentiate between them. To improve the dataset and model, a pulse simulator was introduced as a fourth respiratory state, enhancing the generation of more precise and comprehensive respiratory state data. This enhancement allows the model to more effectively recognize the different respiratory states, thus increasing the robustness and accuracy of classification. The long-term respiratory status monitoring system is designed to be attached to the simulated radial artery of the pulse generator using medical tape, as shown in Fig. S30, with pulse signals continuously collected over a period of 2.8 h (Fig. S31). In the pulse dataset, the three human states exhibit a broader range of pulse rates, whereas the machine-generated pulse rates tend to cluster around 70 bpm, as demonstrated in Fig. S32. This consistency in machine-generated pulse rates can be attributed to the enhanced stability of the machine-generated pulse cycle.

The dataset was constructed using pulse feature data from four respiratory states. BiLSTM models were employed to process the time series of RIAV, RIFV, and RIIV features, aiming to capture contextual information and enhance time series recognition (Fig. S33). However, during the training phase, individual BiLSTM models often experienced suboptimal training and performance due to local optimization, leading to significant fluctuations in accuracy and loss values (Fig. S34). This issue is likely due to the models' tendency to settle into local minima during the optimization process, which adversely affects their generalization capabilities. The integration of a Residual Network (ResNet) effectively mitigated these issues by substantially improving the network's ability to identify relevant features while maintaining the integrity of the training process. This enhancement bolstered the model's training stability and generalization capabilities (Figs. 4g and S35). Figure 4f shows the configuration of the ResNet-BiLSTM network, and Table S2 lists the specific model parameters. The classification accuracy of the ResNet-BiLSTM model reached as high as 99.5% (Fig. 4h). In contrast, the overall accuracy of the BiLSTM model was slightly lower, at 99% (Fig. 4i), particularly in recognizing slow breathing. After integrating the residual network for optimization, the recognition accuracies for the four respiratory states—slow breathing, normal breathing, fast breathing, and simulated breathing—showed significant improvement and a more balanced distribution. The accuracies for each state were 99.7%,

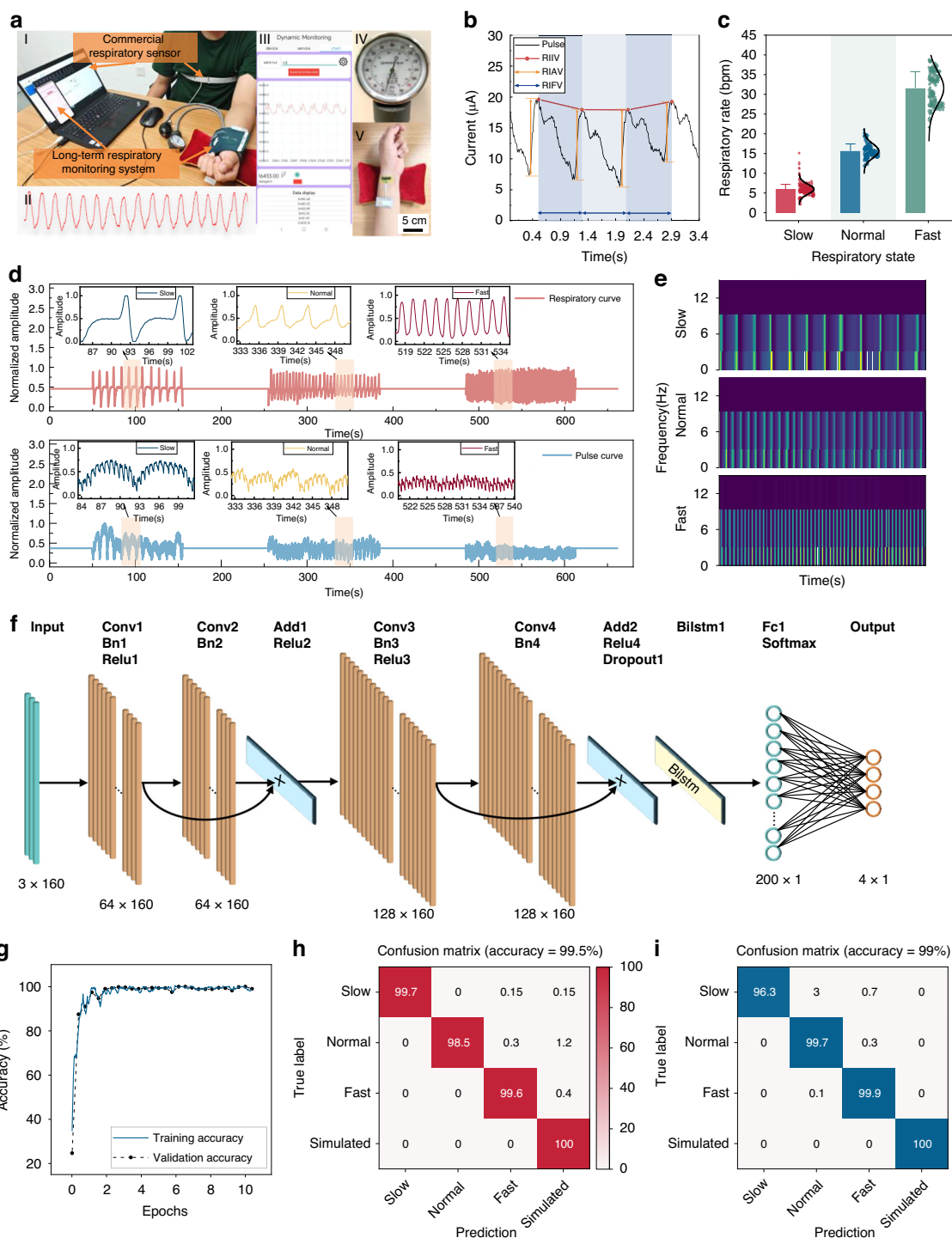


Fig. 4 Pulse and respiration data collection using the flexible sensor system. **a** Real-time acquisition of pulse and respiration signal images. **b** A diagram showing the relationship between pulse characteristics and respiration. **c** A histogram displaying respiratory frequencies across three breathing states: slow, normal, and fast. **d** Pulse and respiration signals for three breathing states: slow, normal, and fast, with enlarged images extracted from the original signals for clarity. **e** A frequency-time representation of the breathing signal across various states over a 100-s period. **f** Introduction of a BiLSTM neural network with a residual module. **g** Training accuracy iteration curve for the ResNet-BiLSTM model. **h** Classification results for a dataset of 2708 cases using the ResNet-BiLSTM model. **i** Classification results for the same dataset of 2708 cases using the BiLSTM model alone

98.5%, 99.6%, and 100%, respectively. The confusion matrices in Fig. S36 display the classification accuracies for the training and test sets of the two models.

The ResNet-BiLSTM model presents a robust tool for the long-term monitoring of respiratory status. For this purpose, a 32-s pulse signal was selected, preprocessed, and its features extracted to serve as input data for the ResNet-BiLSTM model. This model then classifies the respiratory state. The 32-s pulse data is refreshed every 2 s, and following the completion of the processing phase, the most recently classified state is obtained through modeling. This iterative process continuously monitors an individual's respiratory state. In this study, pulse data were collected from six volunteers, each exhibiting three distinct respiratory states: slow, normal, and fast, over a period exceeding 300 s. The ResNet-BiLSTM model, in conjunction with a standalone BiLSTM model, was employed to achieve extended monitoring of respiratory functions. Concurrently, respiratory states identified by commercial respiratory sensors served as reference labels for comparison of outcomes. Figure 5a–d, S37 and S38 depict the results of continuous respiration monitoring for the volunteers, including pulse and respiration imagery during transitions between respiratory states. Specifically, Fig. 5a-II displays 32-s pulse and respiration data corresponding to the yellow-highlighted areas in Fig. 5a-I. Transition points a and b correspond to shifts from slow to normal respiration, while points c and d denote transitions from normal to fast respiration. The ResNet-BiLSTM model, along with the BiLSTM model, demonstrates high accuracy in recognizing mixed respiratory states and effectively mitigates the impact of external disturbances and fluctuations in respiratory state. In contrast, traditional respiratory rate thresholding methods lack the robustness required to manage such sudden changes, often resulting in the incorrect identification of respiratory states. For instance, when monitoring the respiratory state of Volunteer 3 over an extended period, the recognition accuracy of the ResNet-BiLSTM model reached 100%, significantly outperforming the BiLSTM model, as depicted in Fig. 5c. Subsequently, the average classification accuracy for each individual across all respiratory states was analyzed and presented in a radar plot (Fig. 5e). As illustrated in Fig. 5e, the accuracy curve of the ResNet-BiLSTM model exhibits a larger area and a more uniform distribution, indicating superior stability across various conditions. Furthermore, the model demonstrates enhanced robustness compared to the BiLSTM model. To analyze the results of the hierarchical output feature matrix “Bilstm1” depicted by the two models in Figs. 4f and S33, we employed the t-SNE downscaling technique with the objective of visualizing the dataset (Fig. 5f, g). Each data point, representing a specific respiratory state, was mapped from a high-

dimensional feature space to a two-dimensional representation for visualization purposes. Points representing the same respiratory state were grouped into four categories, each labeled with 95% confidence circles. Figure 5g reveals considerable uncertainty in the BiLSTM model's performance, as evidenced by the overlap between the confidence circles.

Conclusion

This study introduces an innovative wearable wrist-worn system designed for the long-term monitoring of respiratory activity. Characterized by its fingerprint-like configuration, the system enhances surface roughness and mechanical adhesion, thereby ensuring sustained sensor performance over extended periods. Weighing only 9 grams, the system significantly alleviates the burden on the user. Furthermore, it utilizes a ResNet-BiLSTM model for respiratory monitoring, achieving a classification accuracy of 99.5%. This compact and highly adaptable system offers precise long-term monitoring of various breathing patterns, an improvement over traditional sensors which may be placed in the mouth, nose, chest, or abdomen and often cause physical and psychological discomfort to users. Integrated with a dedicated mobile application, the system facilitates the quantitative collection and analysis of respiratory data, supporting daily monitoring and health management. This groundbreaking approach is anticipated to play a significant role in the prevention of respiratory diseases and in forming the foundation for clinical treatment decisions.

Methods

Manufacturing of flexible sensors

The manufacturing process of flexible sensors began with the preparation of a TPU particle solution. This involves dissolving 2 grams of TPU sourced from Ruixiang Polymer Material Management Department in Zhangmutou, Dongguan, into 5 milliliters of dimethylformamide (DMF, Aladdin). The mixture was then stirred using a magnetic stirrer (LC-MH Pro, Shanghai Lichen Bangxi Instrument Technology Co., Ltd.) at a temperature of 80 °C and a speed of 800 rpm for 3 h. Subsequently, carbon nanotubes (CNT, Suzhou Carbon Peak Graphene Technology Co., Ltd.) were added, and the stirring continued at 80 °C and 1200 rpm for an additional 6 h. The mixture was then subjected to ultrasonic waves (LC-UC-21, Shanghai Lichen Instrument Technology Co., Ltd) at 80 °C for 1 h to enhance dispersion. Afterward, the mixture was stirred again at 80 °C and 1200 rpm for 2 more h to obtain the sensitive layer solution. Simultaneously, a PDMS solution was prepared by mixing 5 grams of silicone rubber masterbatch with 0.5 grams of hardener (Dow Corning, USA), supplemented by 0.05 grams of pigment, and stirred for 3 min. This mixture was then

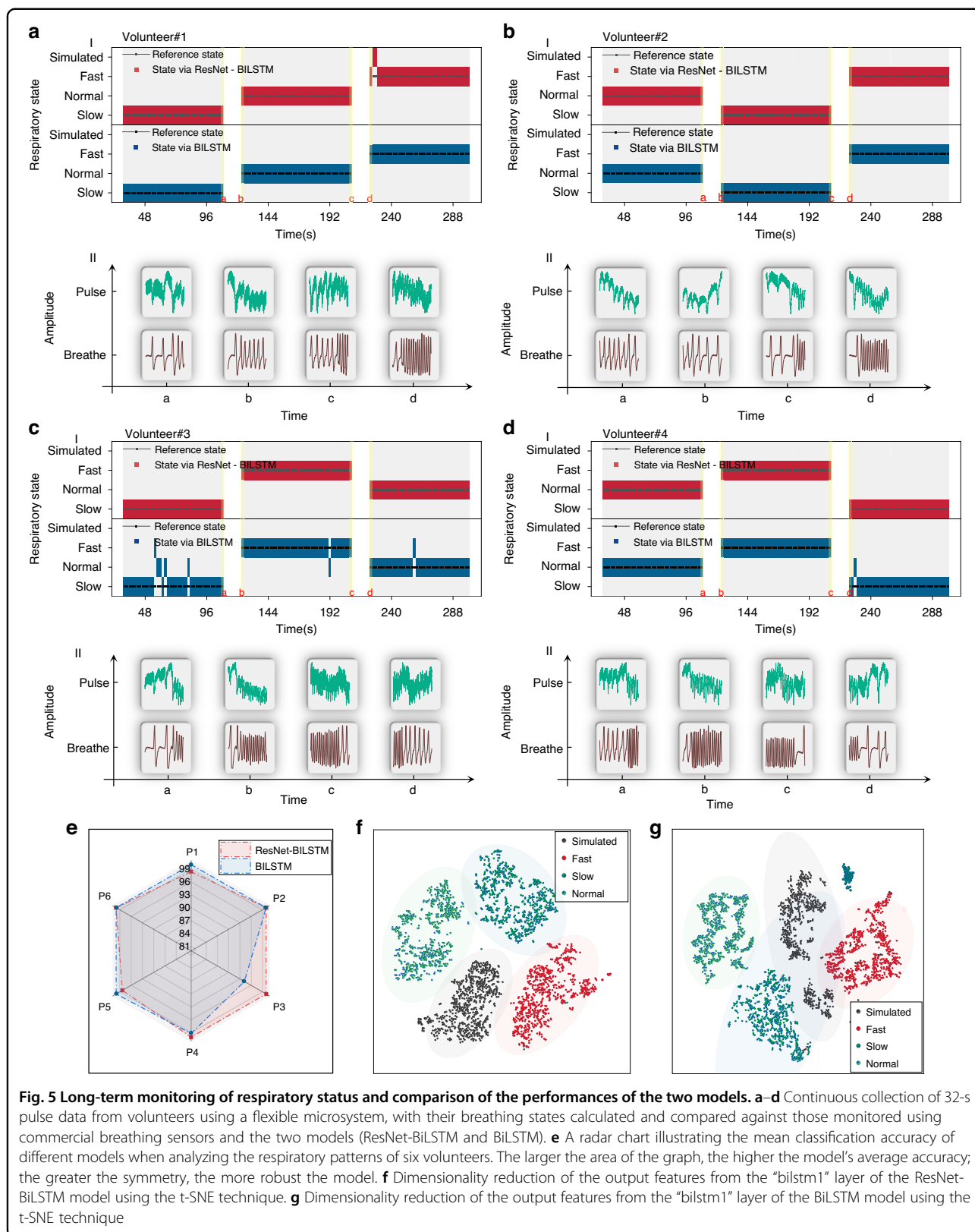


Fig. 5 Long-term monitoring of respiratory status and comparison of the performances of the two models. **a–d** Continuous collection of 32-s pulse data from volunteers using a flexible microsystem, with their breathing states calculated and compared against those monitored using commercial breathing sensors and the two models (ResNet-BiLSTM and BiLSTM). **e** A radar chart illustrating the mean classification accuracy of different models when analyzing the respiratory patterns of six volunteers. The larger the area of the graph, the higher the model’s average accuracy; the greater the symmetry, the more robust the model. **f** Dimensionality reduction of the output features from the “bilstm1” layer of the ResNet-BiLSTM model using the t-SNE technique. **g** Dimensionality reduction of the output features from the “bilstm1” layer of the BiLSTM model using the t-SNE technique

placed in a sealed box and degassed using a vacuum pump (2RS-4, Shanghai Xinyi Instrument Co., Ltd) for 5 min to eliminate any air bubbles. Once degassed, the solution was ready for application. An aluminum plate was cleansed with deionized water and positioned in the center of a Spin Coater (KW-4B, Beijing Saidekesi Electronics Co., Ltd). The PDMS solution was carefully deposited onto the center of the plate, and the Spin Coater was activated for 1 min. Following spinning, the aluminum plate was removed and placed on a hot bench at 80 °C for 6 h to cure the PDMS film.

TPU film (XJU150, 0.05 mm thickness, provided by Shanghai Xingxia Polymer Products Co., Ltd.) was cut into two 8 cm × 8 cm pieces. These pieces were heated at 80 °C for 20 min to facilitate expansion and subsequent size adjustment. Upon cooling, the films were treated in a plasma cleaner (PDC-36G, supplied by Hefei Kejing Material Technology Co., Ltd.) for 1 min to eliminate surface contaminants and small particles, thereby enhancing surface adhesion. The treated TPU films were then affixed onto a screen printing table (equipment provided by Hunan Deyun Printing Equipment Co., Ltd.), and a printing mesh bearing electrode patterns was placed atop the films. Conductive silver paste was screen-printed onto the TPU film using a scraper, followed by a heating step at 80 °C for 5 min to form the electrode layer. The same screen printing method was employed to deposit a sensitive layer solution onto another treated TPU film, which was similarly heated at 80 °C for 5 min to develop the sensitive layer. Subsequently, the TPU film with the electrode pattern was transferred back to the screen printing table, and a TPU solution was applied to establish the spacer layer using the identical printing technique. The two printed TPU films were then aligned such that the sensitive layer completely covered the interdigital electrodes of the electrode layer. A flexible flat cable (40 mm long, 2.5 mm wide, 0.1 mm thick) from a data acquisition module was connected to the electrode layer to facilitate signal acquisition. The assembled layers were placed in a vacuum oven (DZF, manufactured by Hangzhou Mei Instrumentation Technology Co., Ltd.) and heated at 70 °C for 90 min to ensure adhesion between the upper and lower TPU substrates, thus forming semi-finished sensors. A plasma-treated PDMS film was then cut to form the upper PDMS layer, while another plasma-treated PDMS film was etched using a 355 nm ultraviolet laser (YL65U, produced by Wuhan Yuanlu Co., Ltd.) to create a fingerprint-like structure on the lower PDMS layer. The laser etching process was conducted three times at a speed of 1000 mm/s, with a pulse frequency of 60 kHz and a pulse interval of 12 μs. Finally, the sensor was encapsulated using the upper and lower PDMS layers, and the assembly was heat-pressed with a hot press machine (provided by Yiwu Yizhao Machinery Co., Ltd.)

for 1 min at 80 °C. This process bonded the layers together, resulting in the production of a flexible sensor.

Manufacturing of flexible circuit packaging

The process of encapsulating circuits involved the use of inverted mold technology. A silicone base and curing agent (ShinBon408, Dehua County Xinbang Chemical Materials Trading Co., Ltd) were mixed at a ratio of 50:1. Subsequently, a pigment was uniformly incorporated into the mixture to ensure consistent coloration throughout. This mixture was then poured into the mold and subjected to a vacuum defoaming process to eliminate air bubbles. After allowing the mixture to set for 12 h, the silicone underwent a curing process. Upon completion, the mold was opened to reveal the encapsulated circuit, with both upper and lower layers fully formed as shown in Fig. S20.

Morphological characterization of materials

The morphological features of the silver electrode, the sensitive layer, and the fingerprint-like ring structure were examined using a scanning electron microscope (Carl Zeiss AG, G300).

Sensor performance testing

The electromechanical performance of the sensors was evaluated using a digital LCR meter (TH2840B, Tonghui) and a mechanical tester (ZQ-990B, ZhiQu). A variable pressure ranging from 1 to 50 kPa was applied to the sensors, along with a bias potential of 1 V, also administered using the digital LCR meter (TH2840B, Tonghui). Following this, the current output of the sensor was measured to determine its performance indices.

BiLSTM respiratory state classification model

In this study, synchronous pulse and respiration data from 13 volunteers and a machine were collected over a duration of 32 s. The respiration data served as the basis for assigning state labels. The pulse data were pre-processed to derive three distinct time series at a sampling rate of 5 Hz, representing RIAV, RIFV, and RIIV. Each respiratory state—slow breathing, normal breathing, fast breathing, and machine breathing—was represented by 677 instances, cumulating in a total pulse dataset of 2708 cases. To ensure robust model training, the dataset was randomly divided into training, validation, and test sets in a 6:2:2 ratio, respectively.

During the data analysis phase, a BiLSTM network was developed using MATLAB software. The network was configured with 100 neurons in the input layer that received the three distinct feature time sequences: RIAV, RIFV, and RIIV. These inputs were then processed through a fully connected layer, leading to the generation of four output channels corresponding to the four types of

respiratory states: slow respiration, normal respiration, fast respiration, and machine respiration.

Throughout the training process, the actual respiratory states of the subjects were utilized to assess the accuracy of the model's predictions. The performance of the model was incrementally improved through iterative optimization. Comprehensive statistical analyses were performed on the BiLSTM model's continuous prediction results, aiming to evaluate the predictive performance of the model in accurately classifying respiratory states.

ResNet-BiLSTM respiratory state classification model

In this study, we employed the ResNet module to optimize the performance of deep learning networks for respiratory state classification. The model was configured to process three characteristic time series—RIAV, RIFV, and RIIV—each sampled at a frequency of 5 Hz. To prepare for the application of the BiLSTM model, we integrated a residual network with output channels of 64 and 128, while meticulously preserving the integrity of the dataset. This architecture was designed to enhance the network's ability to extract features, thereby improving the stability of the model during training.

After the training phase, we conducted a comprehensive statistical analysis to evaluate the performance of the ResNet-BiLSTM model in the continuous prediction of respiratory states. We compared these results with those obtained from the training phase and with the outcomes from a conventional BiLSTM model. The comparative analysis revealed that the ResNet-BiLSTM model demonstrated superior efficacy in recognizing respiratory states.

Acknowledgements

This research was supported by the National Key Research and Development Program of China (2023YFB3208600), the National Natural Science Foundation of China (No. 62274140), Key Program of the National Natural Science Foundation of China (62433017) and the Science and Technology on Vacuum Technology and Physics Laboratory Fund (HTKJ2023KL510008), the Fundamental Research Funds for the Central Universities (20720230030), the Xiaomi Young Talents Program/Xiaomi Foundation, Shenzhen Science and Technology Program (JCYJ20230807091401003).

Author details

¹Key Laboratory of Instrumentation Science and Dynamic Measurement Ministry of Education, North University of China, Taiyuan 030051, China. ²College of Chemistry and Chemical Engineering, Xiamen University, Xiamen 361105, China. ³Natural Sciences, MAPS Faculty, UCL, Gower Street, London WC1E 6BT, UK. ⁴School of Automation and Software Engineering, Shanxi University, Taiyuan 030006, China. ⁵Pen-Tung Sah Institute of Micro-Nano Science and Technology, Xiamen University, Xiamen 361102, China. ⁶Shenzhen Research Institute of Xiamen University, Xiamen University, Shenzhen 518000, China. ⁷School of Aerospace Engineering, Xiamen University, Xiamen 361102, China. ⁸Science and Technology on Vacuum Technology and Physics Laboratory, Lanzhou Institute of Physics, Chinese Academy of Space Technology, Lanzhou 730000, China

Author contributions

X.Z. and J.C. designed and fabricated the samples, performed the experiments, analyzed the data and wrote the manuscript. L.X. and S.M. carried out the

formal and visual analyses. X.W. and Y.Z. carried out the experiments and compiled the data. C.X. and Y.W. provided conceptual advice. D.C., Z.Z., H.Z. and L.G. conceived and supervised this study. All authors read the manuscript and completed manuscript revisions. All authors have given approval to the final version of the manuscript.

Conflict of interest

The authors declare no competing interests.

Ethical approval

All human subject studies were approved by the Medical Ethics Committee of Xia Men University (Protocol: XDYX202311K70), and the volunteers gave informed consent.

Supplementary information The online version contains supplementary material available at <https://doi.org/10.1038/s41378-025-00924-4>.

Received: 15 November 2024 Revised: 6 March 2025 Accepted: 13 March 2025

Published online: 16 May 2025

References

- Routley, C., Walker, S., Alton, E. W. & Hall, I. P. Fixing lung health in the UK: accelerating respiratory research and innovation. *Thorax* **79**, 809–810 (2024).
- Sayers, I., John, C., Chen, J. & Hall, I. P. Genetics of chronic respiratory disease. *Nat. Rev. Genet.* **25**, 534–547 (2024).
- Holland, A. E. et al. European Respiratory Society clinical practice guideline on symptom management for adults with serious respiratory illness. *Eur. Respir. J.* **63**, 2400335 (2024).
- Shen, S. et al. Advances in wearable respiration sensors. *Mater. Today* **72**, 140–162 (2024).
- Yin, Z. et al. Wearable respiratory sensors for health monitoring. *NPG Asia Mater.* **16**, 8 (2024).
- Lan, B. et al. A highly sensitive coaxial nanofiber mask for respiratory monitoring assisted with machine learning. *Adv. Fiber Mater.* **6**, 1402–1412 (2024).
- Hong, W. Twistable and stretchable nasal patch for monitoring sleep-related breathing disorders based on a stacking ensemble learning model. *ACS Appl. Mater. Interfaces* **16**, 47337–47347 (2024).
- Vicente, B. A., Sebastião, R. & Sencadas, V. Wearable devices for respiratory monitoring. *Adv. Funct. Mater.* **34**, 2404348 (2024).
- Qiu, C., Wu, F., Han, W. & Yuce, M. R. A wearable bioimpedance chest patch for real-time ambulatory respiratory monitoring. *IEEE Trans. Biomed. Eng.* **69**, 2970–2981 (2022).
- Selvakumar, K. et al. Realtime PPG based respiration rate estimation for remote health monitoring applications. *Biomed. Signal Process. Control* **77**, 103746 (2022).
- Motin, M. A., Karmakar, C. K. & Palaniswami, M. Ensemble empirical mode decomposition with principal component analysis: a novel approach for extracting respiratory rate and heart rate from photoplethysmographic signal. *IEEE J. Biomed. Health Inform.* **22**, 766–774 (2018).
- Bondala, V. R. & Komalla, A. R. An efficient model for extracting respiratory and blood oxygen saturation data from photoplethysmogram signals by removing motion artifacts using heuristic-aided ensemble learning model. *Comput. Biol. Med.* **180**, 108911 (2024).
- Laloy-Borgna, G., Puyo, L., Nishino, H., Atlan, M. & Catheline, S. Observation of natural flexural pulse waves in retinal and carotid arteries for wall elasticity estimation. *Sci. Adv.* **9**, eadf1783 (2023).
- Akhmimi, A., Sprung, V. S., Lip, G. Y. H., Oxborough, D. & Shantsila, A. Arterial stiffness assessment in patients with resistant hypertension using pulse wave analysis. *Eur. Heart J.* **44**, ehad655.2305 (2023).
- Hörandtner, C. et al. Attractor reconstruction for quantifying the arterial pulse wave morphology during device-guided slow breathing. *Cardiovasc. Eng. Technol.* **13**, 939–949 (2022).
- Ramirez, A. et al. Assessment of sleep quality by pulse wave amplitude and actigraphy in children with sleep-disordered breathing: evaluation at diagnosis and under non-invasive ventilation. *Sleep. Breath.* **17**, 827–835 (2013).

17. Mengden, T., Bachler, M., Sehnert, W., Marschall, P. & Wassertheurer, S. Device-guided slow breathing with direct biofeedback of pulse wave velocity—acute effects on pulse arrival time and self-measured blood pressure. *Blood Press. Monit.* **28**, 52–58 (2023).
18. Pimentel, M. A. F. et al. Toward a robust estimation of respiratory rate from pulse oximeters. *IEEE Trans. Biomed. Eng.* **64**, 1914–1923 (2017).
19. Charlton, P. H. et al. An assessment of algorithms to estimate respiratory rate from the electrocardiogram and photoplethysmogram. *Physiol. Meas.* **37**, 610–626 (2016).
20. Argüello-Prada, E. J., Marcillo Ibarra, K. D. & Díaz Jiménez, K. L. The use of successive systolic differences in photoplethysmographic (PPG) signals for respiratory rate estimation. *Heliyon* **10**, e26036 (2024).
21. Leier, M., Jervan, G. & Stork, W. Respiration signal extraction from photoplethysmogram using pulse wave amplitude variation. in *2014 IEEE International Conference on Communications (ICC)* 3535–3540 (IEEE, 2014).
22. Song, J., Li, D., Ma, X., Teng, G. & Wei, J. PQR signal quality indexes: a method for real-time photoplethysmogram signal quality estimation based on noise interferences. *Biomed. Signal Process. Control* **47**, 88–95 (2019).
23. Gao, H., Wu, X., Shi, C., Gao, Q. & Geng, J. A LSTM-based realtime signal quality assessment for photoplethysmogram and remote photoplethysmogram. in *2021 IEEE/CVF Conference on Computer Vision and Pattern Recognition Workshops (CVPRW)* 3826–3835 (IEEE, 2021).
24. Ignácz, A., Földi, S., Sótónyi, P. & Cserey, G. NB-SQL: a novel non-binary signal quality index for continuous blood pressure waveforms. *Biomed. Signal Process. Control* **70**, 103035 (2021).
25. He, C. et al. A smart flexible vital signs and sleep monitoring belt based on MEMS triaxial accelerometer and pressure sensor. *IEEE Internet Things J.* **9**, 14126–14136 (2022).
26. Deng, R., Gao, Y., Huang, X., Zhang, L. & Wu, P. A research of the respiratory status detection method measured by abdominal rise and fall. *Heliyon* **9**, e14728 (2023).
27. He, S., Han, Z., Iglesias, C., Mehta, V. & Bolic, M. A real-time respiration monitoring and classification system using a depth camera and radars. *Front. Physiol.* **13**, 799621 (2022).
28. Bokka, N., Karhade, J. & Sahatiya, P. Deep learning enabled classification of real-time respiration signals acquired by MoSSe quantum dot-based flexible sensors. *J. Mater. Chem. B* **9**, 6870–6880 (2021).
29. Zhang, J. et al. Intelligent respiratory status monitoring via a 1DCNN-assisted microfiber sensor. *IEEE Sens. J.* **24**, 19136–19142 (2024).
30. Asatani, N., Kamiya, T., Mabu, S. & Kido, S. Classification of respiratory sounds using improved convolutional recurrent neural network. *Comput. Electr. Eng.* **94**, 107367 (2021).
31. Wall, C., Zhang, L., Yu, Y. & Mistry, K. Deep recurrent neural networks with attention mechanisms for respiratory anomaly classification. in *2021 International Joint Conference on Neural Networks (IJCNN)* 1–8 (IEEE, 2021).
32. Karabayir, I., Akbilgic, O. & Tas, N. A novel learning algorithm to optimize deep neural networks: evolved gradient direction optimizer (EVGO). *IEEE Trans. Neural Netw. Learn. Syst.* **32**, 685–694 (2021).
33. Park, H. et al. High performance flexible micro-supercapacitor for powering a vertically integrated skin-attachable strain sensor on a bio-inspired adhesive. *Nano Energy* **83**, 105837 (2021).
34. Park, W. et al. Skin-integrated wireless odor message delivery electronics for the deaf-blind. *ACS Nano* **17**, 21947–21961 (2023).
35. Tian, S., Wang, L. & Zhu, R. A flexible multimodal pulse sensor for wearable continuous blood pressure monitoring. *Mater. Horiz.* **11**, 2428–2437 (2024).
36. Chen, S. et al. Quantitative and real-time evaluation of human respiration signals with a shape-conformal wireless sensing system. *Adv. Sci.* **9**, 2203460 (2022).
37. Fekr, A. R., Janidarmian, M., Radecka, K. & Zilic, Z. Respiration disorders classification with informative features for m-Health applications. *IEEE J. Biomed. Health Inform.* **20**, 733–747 (2016).
38. Hong, J.-W., Kim, S.-H. & Han, G.-T. Detection of multiple respiration patterns based on 1D SNN from continuous human breathing signals and the range classification method for each respiration pattern. *Sensors* **23**, 5275 (2023).
39. Wang, S. et al. An integrated flexible self-powered wearable respiration sensor. *Nano Energy* **63**, 103829 (2019).
40. Li, Y. et al. Graphdiyne-based flexible respiration sensors for monitoring human health. *Nano Today* **39**, 101214 (2021).
41. Park, S. W., Das, P. S., Chhetry, A. & Park, J. Y. A flexible capacitive pressure sensor for wearable respiration monitoring system. *IEEE Sens. J.* **1** <https://doi.org/10.1109/JSEN.2017.2749233> (2017).
42. Ye, L. et al. Face mask integrated with flexible and wearable manganite oxide respiration sensor. *Nano Energy* **112**, 108460 (2023).
43. Li, B. et al. A flexible humidity sensor based on silk fabrics for human respiration monitoring. *J. Mater. Chem. C* **6**, 4549–4554 (2018).
44. Liu, Z. et al. Flexible piezoelectric nanogenerator in wearable self-powered active sensor for respiration and healthcare monitoring. *Semicond. Sci. Technol.* **32**, 064004 (2017).
45. Zhou, C. et al. Rapid response flexible humidity sensor for respiration monitoring using nano-confined strategy. *Nanotechnology* **31**, 125302 (2020).
46. Wang, X. et al. An ultrafast-response and flexible humidity sensor for human respiration monitoring and noncontact safety warning. *Microsyst. Nanoeng.* **7**, 99 (2021).
47. Teng, Y. et al. Fully printed minimum port flexible interdigital electrode sensor arrays. *Nanoscale* **16**, 7427–7436 (2024).
48. Li, J. et al. Thin, soft, wearable system for continuous wireless monitoring of artery blood pressure. *Nat. Commun.* **14**, 5009 (2023).
49. Yao, C. et al. Personalized machine learning-coupled nanopillar triboelectric pulse sensor for cuffless blood pressure continuous monitoring. *ACS Nano* **17**, 24242–24258 (2023).